

1 Surface-temperature and surface-layer turbulence in a convective
2 boundary layer

3 Anirban Garai^a, Eric Pardyjak^b, Gert-Jan Steeneveld^c, and Jan Kleissl^{a,1}

4 ^aDept of Mechanical and Aerospace Engineering, University of California, San Diego

5 ^bDept of Mechanical Engineering, University of Utah

6 ^cMeteorology and Air Quality, Wageningen University, Netherlands

7

8

¹ *Corresponding author address:* Jan Kleissl, Department of Mechanical and Aerospace Engineering, University of California, San Diego, 9500 Gilman Drive, EBU11 – 580, La Jolla, CA 92093-0411. E-mail: jkleissl@ucsd.edu

9 Abstract

10 Previous laboratory and atmospheric experiments have shown that turbulence influences the
11 surface-temperature in a convective boundary layer. The main objective of this study is to examine
12 land-atmosphere coupled heat transport mechanism for different stability conditions. High frequency
13 infrared imagery and sonic anemometer measurements were obtained during the Boundary Layer Late
14 Afternoon and Sunset Turbulence (BLLAST) experimental campaign. Temporal turbulence data in
15 the surface-layer are then analyzed jointly with spatial surface-temperature imagery.

16 The surface-temperature structures (identified using surface-temperature fluctuations) are
17 strongly linked to atmospheric turbulence as manifested in several findings. The surface-temperature
18 coherent structures move at an advection speed similar to the upper surface-layer or mixed-layer
19 wind-speed, with a decreasing trend with increase in stability. Also, with increasing instability the
20 streamwise surface-temperature structure size decreases and the structures become more circular. The
21 sequencing of surface- and air-temperature patterns is further examined through conditional
22 averaging. Surface heating causes the initiation of warm ejection events followed by cold sweep
23 events that result in surface cooling. The ejection events occur about 25% of the time, but account for
24 60 to 70% of the total sensible heat-flux and cause fluctuations of up to 30% in the ground heat-flux.
25 Cross-correlation analysis between air- and surface-temperature confirms the validity of a scalar
26 footprint model.

27 Keywords: Atmospheric surface-layer, Convective boundary layer, Infra-red imagery, Surface-layer
28 plumes, Surface-temperature.

29 1. Introduction

30 The fluid temperature trace in turbulent heat transfer over a flat surface shows the
31 characteristics of periodic activities comprised of alternating large fluctuations and periods of
32 quiescence (Townsend, 1959; Howard, 1966). Sparrow et al. (1970) observed that these periodic
33 activities are due to mushroom-like structures of ascending warm fluid caused by instability due to
34 buoyant forcing (Howard, 1966). Similar structures consisting of ascending warm fluid are also
35 observed in the surface-layer of a convective boundary layer (CBL) and known as surface-layer
36 plumes. These plumes have diameters on the order of the surface-layer height, advection velocities
37 close to the average wind-speed over their depth, are tilted by about 45° due to wind shear, and are
38 responsible for the majority of total momentum and heat transport (Kaimal and Businger, 1970;
39 Wyngaard et al. 1971; Kaimal et al. 1976; Wilczak and Tillman, 1980; Wilczak and Businger, 1983;
40 Renno et al. 2004). As these plumes ascend through the CBL, they combine with each other to create
41 thermals in the mixed-layer.

42 Conditional averaging of surface-layer plumes by Schols (1984) and Schols et al. (1985)
43 revealed that the resulting air-temperature trace shows ramp-like patterns. Gao et al. (1989), Paw U et
44 al. (1992), Braaten et al. (1993) and Raupach et al. (1996) studied these temperature ramp patterns
45 over different canopies and modelled the transport process using the surface renewal method. The
46 surface renewal method conceptualizes the heat exchange process to occur based on coherent
47 structures: a cold air parcel descends to the ground during the sweep event, while it remains close to
48 the ground it is heated, and when it achieves sufficient buoyancy the warm air parcel ascends during
49 the ejection event. The surface renewal method has been successfully employed to estimate sensible
50 and latent heat-fluxes over different canopies by Paw U et al. (1995), Snyder et al. (1996), Spano et al.
51 (1997, 2000), Castellvi et al. (2002), Castellvi (2004) and Casstellvi and Snyder (2009).

52 The effect of coherent structures on the surface-temperature was first observed by Derksen
53 (1974) and Schols et al. (1985) who found streaky patterns of surface-temperature with about a 2°C
54 heterogeneity along the wind-direction using an airborne thermal infra-red (IR) camera. Hetsroni and
55 Rozenblit (1994), Hetsroni et al. (2001), and Gurka et al. (2004) observed a similar streaky structure
56 in surface-temperature in a laboratory convective water flume experiment at different Reynolds
57 numbers. High surface-temperature streaks corresponded to low velocity fluid streaks in the boundary
58 layer and the distance between streaks increased with Reynolds number. Using an IR temperature
59 sensor Paw U et al. (1992), Katul et al. (1998) and Renno et al. (2004) observed surface-temperature
60 fluctuations in the CBL with an amplitude of 0.5°C over 2.6-m high maize crops, greater than 2°C
61 over 1-m high grass, and $2 - 4^{\circ}\text{C}$ over a desert area, respectively. Using IR imagery, Ballard et al.
62 (2004), Vogt (2008) and Christen et al. (2012) observed spatial heterogeneities in the magnitude of

63 surface-temperature fluctuations over a grass canopy, a bare field, and in an urban environment,
64 respectively.

65 Direct numerical simulation (DNS) of turbulent heat transfer coupled with heat conduction in
66 the adjacent solid by Tiselj et al. (2001) revealed that the magnitude of surface-temperature
67 fluctuations depends on the wall thickness and relative strength of thermal response times for the solid
68 and fluid. Balick et al. (2003) identified similar key parameters for the coupled heat transfer process at
69 the earth's surface. Hunt et al. (2003) observed different forms of coherent structures (plumes and
70 puffs) by varying the surface thermal properties in their DNS of the solid-fluid coupled turbulent heat
71 transport process. Ballard et al. (2004) hypothesized that high frequency surface-temperature
72 fluctuations are caused by turbulent mixing. Katul et al. (1998) and Renno et al. (2004) argued that
73 surface-temperature fluctuations are caused by inactive eddy motion and convective mixed-layer
74 processes. Christen and Voogt (2009, 2010) visualized the spatial surface-temperature field in a
75 suburban street canyon and qualitatively attributed the vertical heat transport to the observed coherent
76 structures that were shown to move along the wind-direction.

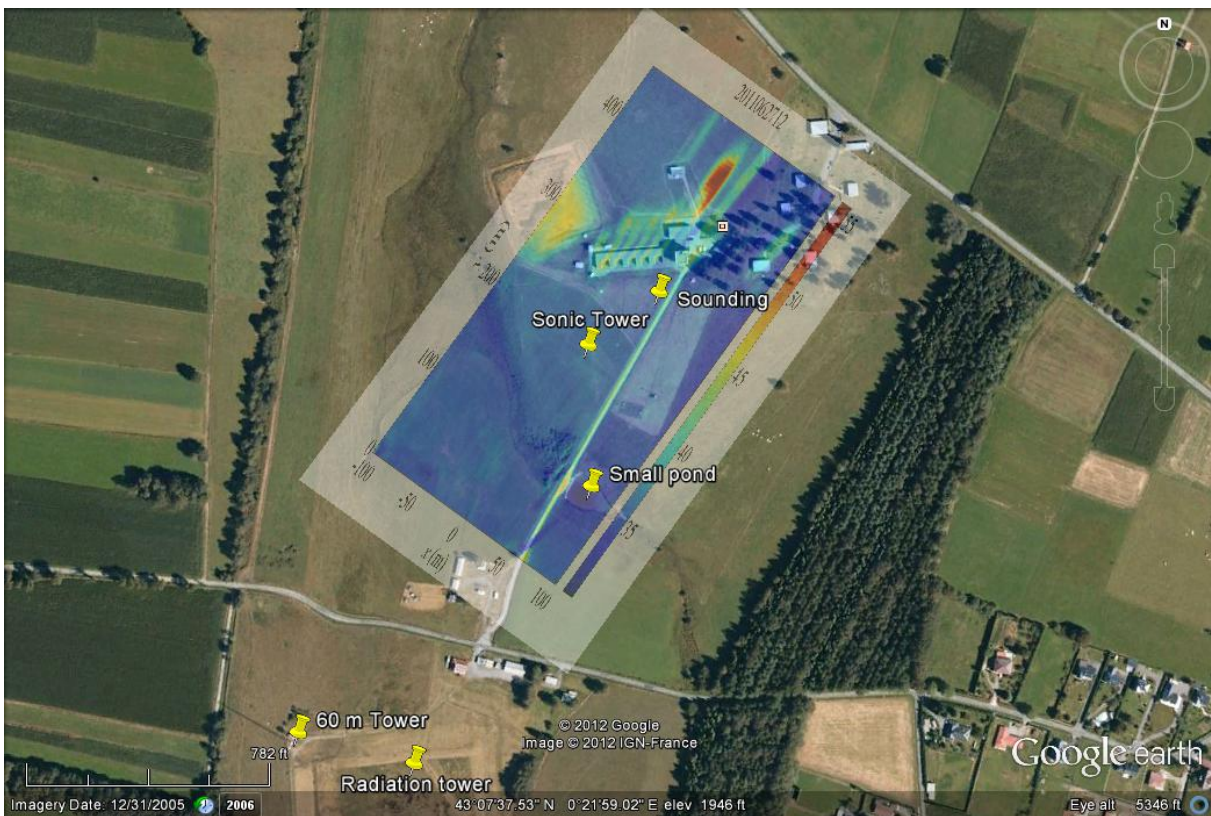
77 Garai and Kleissl (2011) examined surface-temperature structures and heat transport
78 processes over an artificial turf field using 1-Hz IR imagery. Although the camera field-of-view was
79 smaller (48 m x 15 m) than the scale of the largest surface-temperature structures, different surface-
80 temperature characteristics were identified corresponding to different phases of the surface renewal
81 process. The surface-temperature field showed large cold structures during sweep events, small
82 patches of warm structures in a cold background during the transition from sweep to ejection, large
83 warm structures during the ejection events, and small patches of cold structures in a warm background
84 during the transition from ejection to sweep. Sequential animation of the surface-temperature showed
85 growth and merging of thermal footprints moving along the wind-direction. Garai and Kleissl (2011)
86 speculated that these atmospheric turbulence driven surface-temperature fluctuations can induce
87 physical "noise" in different applications of remote sensing, such as the identification of land mines,
88 illegal land-fills and the determination of evapotranspiration for irrigation management. For example,
89 several remote sensing models (e.g. the Surface Energy Balance Algorithm for Land (SEBAL) by
90 Bastiaanssen et al., 1998a,b) estimate sensible heat-flux and evapotranspiration using Monin-
91 Obukhov similarity theory, which relies on mean differences between the surface- and air-
92 temperatures. Thus, the substantial deviation of instantaneous surface-temperature measurement by
93 remote sensing platforms from the true mean can degrade the accuracy of local evapotranspiration
94 estimates. The main objective for the present experimental set-up was to address the main limitation
95 of Garai and Kleissl (2011) by increasing the small field-of-view of the IR camera. Furthermore
96 turbulence measurements were collocated at different heights that allowed further investigation of the
97 cause and manifestation of surface-temperature structures as a function of atmospheric stability and

98 the interaction between thermal footprints and lower surface-layer turbulence. In Sects. 2, 3, and 4 we
99 describe the experimental set-up, results, and discussion and conclusions, respectively.

100 2. Experiment and data processing

101 a. Experimental set-up

102 The experiment was conducted as a part of the Boundary Layer Late Afternoon and Sunset
103 Turbulence (BLLAST; Lothon et al., 2012) field campaign at the Centre de Recherches
104 Atmosphériques, Lannemezan, France from 14 June to 8 July, 2011 (Fig. 1). Surface-temperature data
105 at 1 Hz were captured by a FLIR A320 Thermal IR camera. It was mounted 59 m above ground level
106 (a.g.l.) at the 60-m tower (43°07'25.15" N, 0°21'45.33" E) looking towards 55° N with an inclination
107 of 2° from 16 June to 29 June, 2011. The camera overlooked a 90-mm high grass field with an albedo
108 of 0.19. Longwave radiation (8 – 14 μm wavelength) from the surface was measured over 240 x 320
109 pixels and converted into surface temperature (T_s) assuming an emissivity of 0.95 (Oke, 1987). The
110 accuracy of the camera is ± 0.08 K. A coordinate system transformation and interpolation was
111 performed to transform the original image to a Cartesian coordinate system. This resulted in a camera
112 field-of-view of 450 m x 207 m with a uniform resolution of 4.5 m x 0.65 m. A 1-hr daytime average
113 of the surface-temperature from the IR camera (overlaid on a map in Figure 1) shows road, buildings
114 and bare soil regions to be warmer and a small pond to be cooler than the grass regions.



115

116 Figure 1. Google Earth map of the experimental site. The locations of the 10-m sonic anemometer
 117 tower, 60-m tower, radiation tower, and release position of radiosondes are marked. 1-hr averaged
 118 surface-temperature as viewed from the 60-m tower at 1200 – 1259 UTC (1400 – 1459 local time) on
 119 27 June, 2011 is overlaid. The quantitative analysis considers only the area of $y < 275$ m.

120 Four Campbell Scientific sonic anemometer-thermometers (CSAT) measured the turbulent
 121 velocity components (u , v , w) and sonic air-temperature (air-temperature, T_a) at 20 Hz at 2.23 m, 3.23
 122 m, 5.27 m and 8.22 m a.g.l. inside the camera field-of-view at 43°07'39.2" N, 0°21'37.3" E ("Sonic
 123 Tower" in Fig. 1). Hereinafter these CSATs will be referred to as the 2-m, 3-m, 5-m and 8-m CSATs.
 124 The CSATs were pointing towards 60° N. A coordinate system rotation was conducted to ensure
 125 $|\langle w \rangle / M| < 1\%$ (angled brackets denote temporal averaging and M is the horizontal wind speed) and
 126 to orient the CSAT winds into the IR-camera coordinate system following Wilczak et al. (2001).

127 Radiosondes were released at 43°07'41" N, 0°22'01" E ("Sounding" in Fig. 1) every six
 128 hours until 25 June, 2011 and every three hours thereafter providing profiles of wind speed, direction,
 129 temperature, humidity up to 20 km with a vertical resolution of 5 m. A radiation measurement tower
 130 at 43°07'26" N, 0°21'50.4" E near the 60-m tower (Figure 1) was equipped with Kipp & Zonen
 131 CM22 and CM21 pyranometers to measure the shortwave upwelling and downwelling irradiances,
 132 and Eppley-PIR and Kipp & Zonen CG4 pyrgeometers to measure the longwave upwelling and
 133 downwelling irradiance respectively. All radiation measurements were reported as 1-min averages.
 134 All measurement platforms were GPS synchronized to Coordinated Universal Time (UTC), which
 135 lags local time by two hours.

136 b. Data processing

137 Ogive tests (Foken et al., 2006) revealed that an averaging period of 5 min is sufficient to
 138 estimate momentum- and heat-fluxes from the 2-m to 8-m CSATs using the eddy-covariance method
 139 (for details see the Appendix). To minimize the effects of changing meteorological conditions on the
 140 time series of fluctuating wind speed (u , v , w), air-temperature (T_a), and surface-temperature (T_s) the
 141 5-min linear trend was removed using

$$142 \quad X' = X(t) - (\langle X \rangle_{5min} - a_{X,5min} t), \quad (1)$$

143 where $a_{X,5min}(t)$ is the linear time dependence coefficient of variable X (for surface-temperature,
 144 $a_{T_s,5min}(t, x, y)$, i.e. it is computed separately for each camera pixel). Since, there were no continuously
 145 functioning finewire thermocouples or infra-red gas analyzers on the sonic tower, the kinematic
 146 sensible heat-flux was estimated using

$$147 \quad \frac{H}{\rho_a c_{p,a}} \approx \frac{\langle w' T_a' \rangle}{(1+0.06/B)}, \quad (2a)$$

148 where ρ_a , $C_{p,a}$ and B are the dry air density, dry air specific heat and the Bowen ratio estimated using a
 149 CSAT and a LICOR 7500A CO₂/H₂O analyzer mounted at 29.3 m a.g.l. at the 60-m tower, operated at
 150 10 Hz, and taking an averaging period of 10 min. The 2-m CSAT data were used to estimate the mean
 151 sensible heat-flux defined by Eq. 2a); the friction velocity (Eq. 2b), the convective velocity (Eq. 2c), ;
 152 the surface-layer temperature scale (Eq. 2d),

$$153 \quad u_* = (\langle u'w' \rangle^2 + \langle v'w' \rangle^2)^{1/4} \quad (2b);$$

$$154 \quad w_* = \left(\frac{gz_i}{\langle T_a \rangle} \frac{H}{\rho_a C_{p,a}} \right)^{1/3} \quad (2c)$$

$$155 \quad T_*^{SL} = -\frac{\left(\frac{H}{\rho_a C_{p,a}} \right)}{u_*} \quad (2d); \text{ the Obukhov length, } L = -\frac{\langle T_a \rangle u_*^3}{\kappa g \left(\frac{H}{\rho_a C_{p,a}} \right)} \quad (2e); \text{ and the flux Richardson number,}$$

$$156 \quad Ri_f = \frac{g}{u_*^2} \frac{\left(\frac{H}{\rho_a C_{p,a}} \right)}{\frac{\partial \langle M \rangle}{\partial z}} \quad (2f); \text{ where } \kappa \text{ and } g \text{ are the von Kármán constant (= 0.4) and the acceleration due to}$$

157 gravity respectively. The vertical gradient of horizontal wind-speed was estimated using the Businger-
 158 Dyer similarity relationships.

159 Footprint functions estimate the relative contribution of scalar sources from different ground
 160 locations to the measurement location of the scalar. To calculate the footprints of different CSATs, we
 161 used the scalar footprint derived from the flux footprint model of Hsieh et al. (2000). In this model,
 162 temperature is treated as a passive scalar and the 1-D flux footprint function (f) for the unstable
 163 boundary layer is

$$164 \quad f(\tilde{x}, z_m) = \frac{1}{\kappa^2 \tilde{x}^2} 0.28 z_u^{0.59} |L|^{1-0.59} \exp\left(\frac{-1}{\kappa^2 \tilde{x}} 0.28 z_u^{0.59} |L|^{1-0.59}\right), \quad (3a)$$

165 where \tilde{x} , z_m and z_u are the streamwise distance from the measurement tower, the measurement height
 166 and a scaled measurement height defined as $z_u = z_m (\log(z_m/z_o) - 1 + z_o/z_m)$, where z_o is the
 167 roughness length. The flux footprint (f) is related to scalar footprint (C) by (Kormann and Meixner,
 168 2001)

$$169 \quad M \frac{\partial C}{\partial \tilde{x}} = -\frac{\partial f}{\partial z}. \quad (3b)$$

170 The 1-D scalar footprint function (C) was then used to calculate the 2-D scalar footprint function
 171 (C_{2D}) assuming a Gaussian distribution of zero mean and standard deviation of the wind-direction (σ_θ)
 172 using

$$\sigma_y = \frac{\sigma_\theta \tilde{x}}{1 + \sqrt{\frac{\tilde{x}}{400 \langle M \rangle}}}$$

173 , (3c)

$$174 \quad C_{2D} = \frac{C}{\sqrt{2\pi}\sigma_{\tilde{y}}} e^{-\frac{\tilde{y}^2}{2\sigma_{\tilde{y}}^2}}, \quad (3d)$$

175 where \tilde{y} is the spanwise distance. For the comparison of 20-Hz turbulence data with 1-Hz footprint
 176 averaged surface-temperature data, a box filter of size 1 s centred at the time stamp of the surface-
 177 temperature measurement was applied on the turbulence data. Net radiation R_{net} was obtained from the
 178 radiation tower measurements, but upwelling longwave irradiance measured at the radiation tower
 179 was replaced by the average IR-camera measurement.

180 Finally, the ground heat-flux G was modelled numerically by solving the transient 3-D heat
 181 conduction equation

$$182 \quad \frac{\partial T_g}{\partial t} = \alpha_g \left(\frac{\partial^2 T_g}{\partial x^2} + \frac{\partial^2 T_g}{\partial y^2} + \frac{\partial^2 T_g}{\partial z^2} \right), \quad (4a)$$

183 where α_g and T_g are the thermal diffusivity and the temperature of the soil respectively. The
 184 conduction equation was discretized horizontally using a spectral method with periodic boundary
 185 conditions; vertically a second-order finite difference scheme was used; the Euler implicit scheme was
 186 applied for time integration. The numerical solution of Eq. 4a was validated against the analytical
 187 solutions of constant and sinusoidally varying surface-temperature (not shown). To simulate soil
 188 temperatures, homogeneous clay soil with 40% volumetric water content was assumed yielding
 189 thermal diffusivity α_g and conductivity k_g of $0.4 \text{ mm}^2 \text{ s}^{-1}$ and $0.8 \text{ W m}^{-1} \text{ K}^{-1}$ respectively (Campbell
 190 and Norman, 1998). The IR temperature (T_s) was used as top-surface boundary condition ($z = 0$), an
 191 adiabatic boundary condition ($\frac{\partial T_g}{\partial z} = 0$) was used as the bottom boundary condition ($z = -5.5 \text{ m}$) and
 192 the temperature in the domain was initiated by

$$193 \quad T_g(x, y, z, t = 0) = T_\infty + \frac{\langle G \rangle}{k_g} \left\{ 2 \left(\frac{\alpha_g \tau}{\pi} \right)^{1/2} \exp\left(-\frac{z^2}{4\alpha_g \tau}\right) + \frac{z}{2} \operatorname{erfc}\left(-\frac{z}{2\sqrt{\alpha_g \tau}}\right) \right\}, \quad (4b)$$

194 where $\langle G \rangle (= \langle R_{net} - (1 + \frac{1}{B})H \rangle)$, 4c) the mean ground heat-flux obtained from the surface energy
 195 balance; $\tau (= \left[\frac{k_g \langle (T_s) - T_\infty \rangle}{2\langle G \rangle} \right]^2 \frac{\pi}{\alpha_g})$, 4d) a dummy time variable to minimize unrealistic initialization
 196 effects (Carslaw and Jaeger, 1959); $T_\infty (= 288 \text{ K}$, which is the annual average air-temperature) the soil
 197 temperature as $z \rightarrow -\infty$; and erfc the complimentary error function. As the temperature gradient is
 198 largest near the surface, the vertical grid resolution was set to 1.5 mm; below $z = -0.05 \text{ m}$ the vertical
 199 grid was stretched uniformly to 0.1-m resolution. The simulation was spun up for 100 timesteps to
 200 limit the influence of the initial conditions. The ground heat-flux G then computed from T_g as

$$G = \left[\frac{\Delta z}{2\Delta t} \int_{\Delta t} \rho_g C_{pg} \frac{\partial T_g}{\partial t} dt \right] - \left[\frac{\Delta z}{2\Delta x} \int_{\Delta x} k_g \frac{\partial^2 T_g}{\partial x^2} dx + \frac{\Delta z}{2\Delta y} \int_{\Delta y} k_g \frac{\partial^2 T_g}{\partial y^2} dy \right] + \left[k_g \frac{T_s - T_{g,-\Delta z}}{\Delta z} \right], \quad (4e)$$

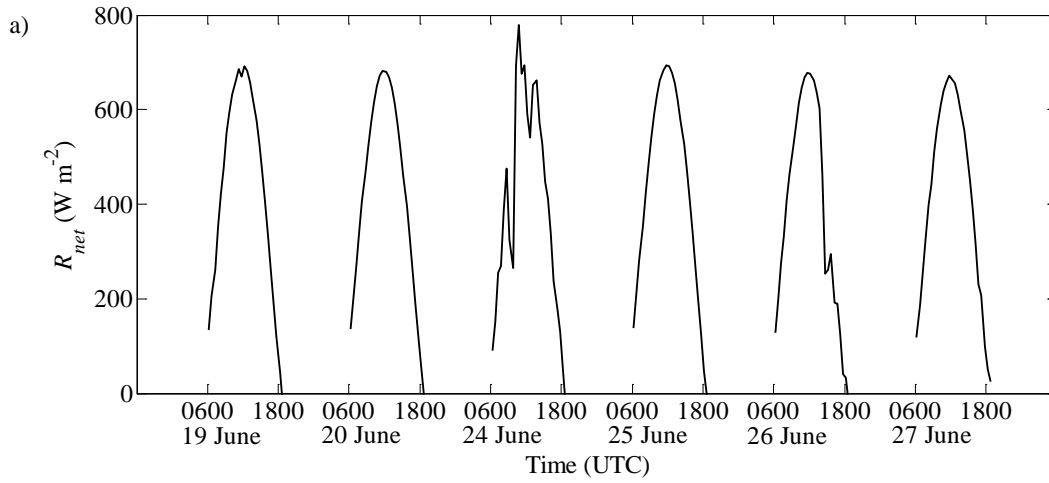
where ρ_g , C_{pg} , Δx , Δy , Δz are density, specific heat of the soil, and grid size in the horizontal (x , y) and vertical (z) directions respectively. In Eq. 4e the first, second and third bracketed terms represent temporal storage, horizontal heat diffusion and vertical heat diffusion respectively.

3. Results

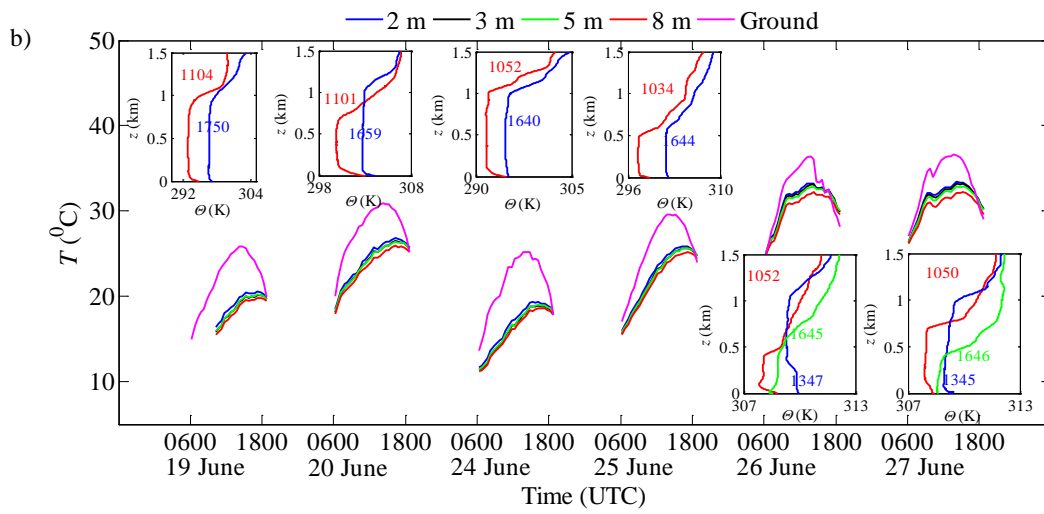
Since the surface-temperature fluctuations only exceed the noise level of the camera during unstable conditions (Garai & Kleissl 2011), only daytime data were considered for detailed analysis. Building ($y > 275$ m) and road (a straight line from $x = 65$ m at $y = 0$ to $x = 30$ m at $y = 300$ m) pixels (Fig. 1) in the IR images were omitted from the analysis, to minimize the effects of surface heterogeneity.

a. Meteorological conditions

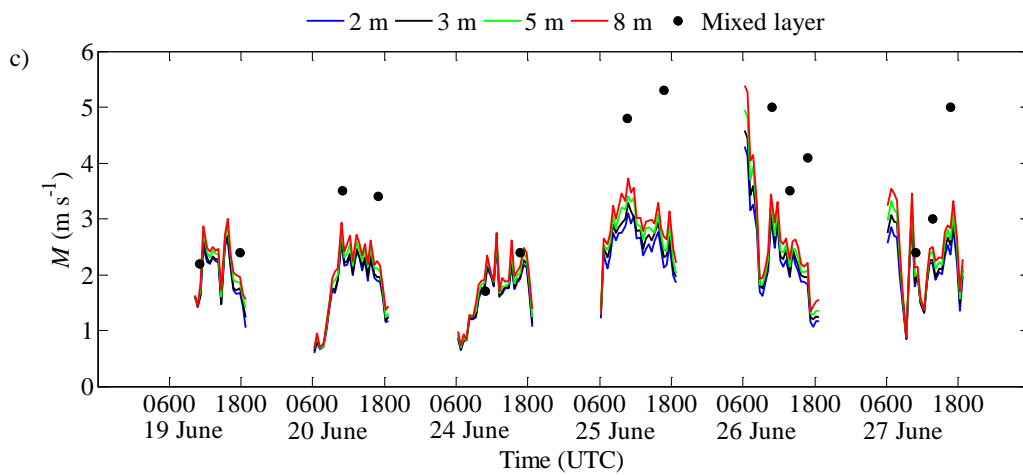
Figure 2 presents 30-min averaged meteorological conditions for the intensive observational periods consisting of the clear days during 16 to 27 June, 2011. Potential temperature from radiosonde data are shown in the inset of the figures. Clear days are expected to produce both stationary time periods and the most unstable stability conditions; R_{net} reaches 700 W m^{-2} at midday for all clear days. There were some early morning and late afternoon cloud periods on 24 and 26 June, respectively, and rain (about 2 – 2.5 mm) occurred on 18 and 22 – 23 June as cold-fronts from the Atlantic Ocean crossed the site. Air-temperature fell to 15 – 20 °C just after the rain and increased on successive clear days. Surface-temperature followed a similar trend as air-temperature. Potential temperature (θ) profiles from radiosondes show that the inversion height (z_i) did not exhibit a strong diurnal cycle except on 20, 26 and 27 June. The height z_i was about 1 km for 19 and 24 June and 600 m for 25 June. It increased from 750 m to 1 km on 20 June, increased from 500 m to 1 km and then fell to 750 m on 26 June, and increased from 750 m to 1 km and then fell to 450 m on 27 June for the 1050, 1350, and 1650 UTC soundings, respectively. The near-surface ($z < 8$ m) wind-speed was about 2.5 m s^{-1} for 19, 20 and 24 June and about 3 m s^{-1} for 25 to 27 June. Mixed-layer wind-speed (the mean of radiosonde data from $z/z_i = 0.1$ to 0.8) was close to the 8 m wind-speed for all days except 25 and 26 June, when the mixed-layer wind-speed was at least 25% larger. Wind-direction was northerly for 19 and 24 June, easterly for 25 and 26 June and north-easterly for 20 and 27 June. Easterly to north-easterly wind are typical for the mountain-plain circulation in the area.



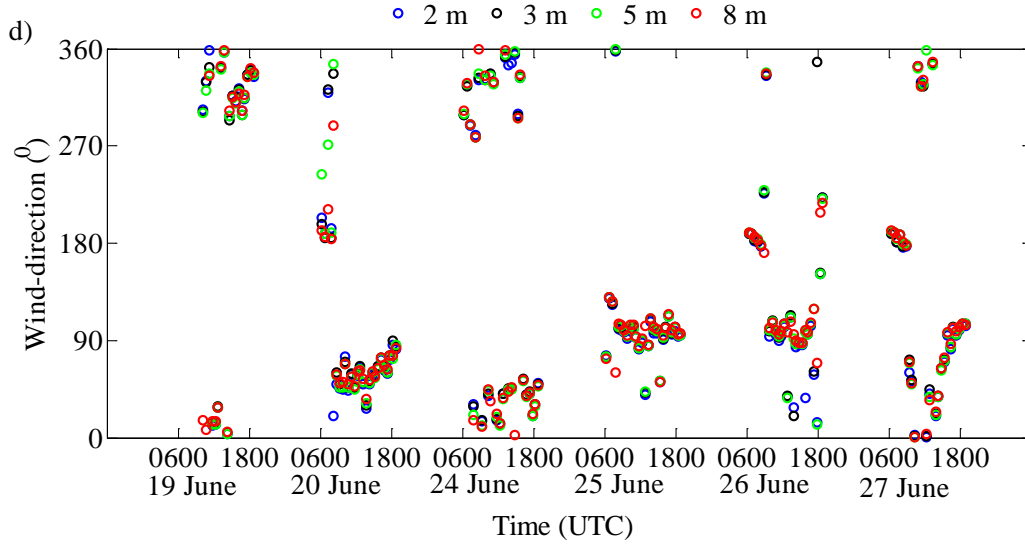
230



231



232



233

234 Figure 2. 30-min averages of (a) net radiation, (b) temperatures, (c) wind-speed and (d) wind-
 235 direction. Radiosonde potential temperature profiles are shown in the inset of (b), where the release
 236 time (HHMM UTC) is shown in colour.

237 30-min periods were chosen for further investigation based on the following stationarity
 238 criteria applied to the 2-m CSAT data: constant Obukhov length, constant wind-speed (standard
 239 deviation of the six consecutive 5-min means is less than 10% of the 30-min mean) and constant
 240 wind-direction (standard deviation of the six consecutive 5-min wind-direction is less than 20°). Data
 241 from the days after the rain (19 and 24 June) were excluded, as the IR surface-temperature was
 242 affected by local pooling of water. Stationary periods are characterized in Table 1 in order of
 243 increasing stability. The data from the 2-m CSAT, indicate that $Ri_f = 1.69\zeta$ with 99.7% coefficient of
 244 determination, where $\zeta = z/L$, with $z = 2.23$ m. For the remainder of the paper, we have chosen ζ to
 245 parameterize the stability.

246 Table 1. Scales, stability and turbulence parameters sorted by L and Ri_f during periods classified as
 247 stationary (see text for criteria used). Inversion heights z_i were estimated visually from the radio
 248 soundings as inflection point in the potential temperature profiles (increase in potential temperature
 249 exceeds 1 K over 100 m height).

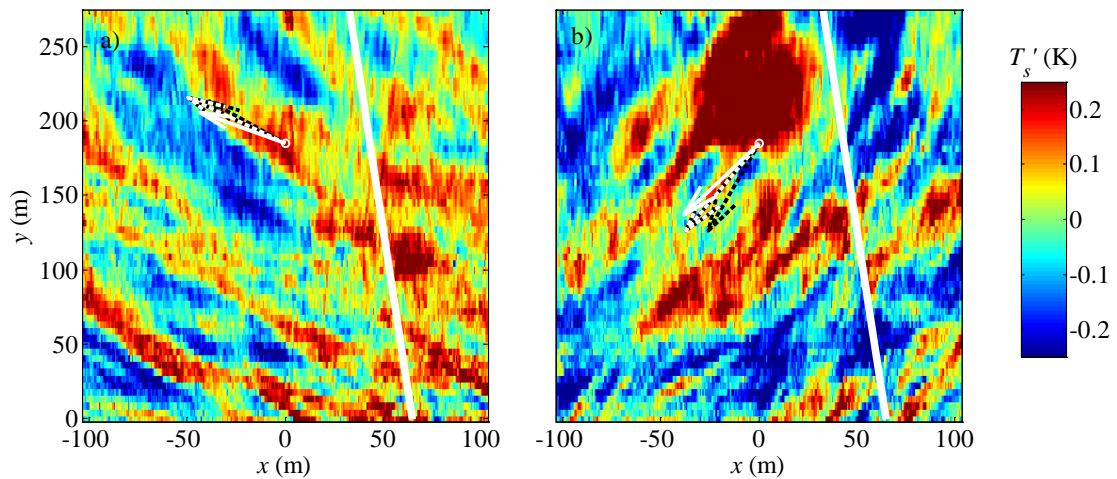
Time (UTC)	L (m)	Ri_f	\mathbf{u}_* (m s ⁻¹)	\mathbf{w}_* (m s ⁻¹)	$\frac{H}{\rho_a c_{p,a}}$ (K m s ⁻¹)	z_i (km)
0930-1000, 27 June	-5.5	-0.66	0.15	0.95	0.045	0.6
0830-0900, 26 June	-6.7	-0.52	0.15	0.71	0.028	0.4
1100-1130, 20 June	-7.3	-0.47	0.22	1.38	0.113	0.7

1100-1130, 27 June	-8.5	-0.39	0.19	1.15	0.058	0.8
1030-1100, 27 June	-8.5	-0.39	0.18	1.06	0.053	0.7
1530-1600, 20 June	-8.8	-0.37	0.19	1.31	0.062	1.1
0935-1005, 26 June	-9.4	-0.35	0.17	0.82	0.043	0.4
0825-0855, 27 June	-10.4	-0.31	0.15	0.76	0.027	0.5
1200-1230, 25 June	-11.7	-0.27	0.26	1.23	0.112	0.5
1030-1100, 25 June	-12.5	-0.25	0.27	1.23	0.112	0.5
0900-0930, 25 June	-14.3	-0.21	0.27	1.18	0.098	0.5
1000-1030, 25 June	-14.7	-0.20	0.28	1.22	0.109	0.5
0830-0900, 25 June	-15.6	-0.19	0.26	1.10	0.079	0.5
1000-1030, 26 June	-19.5	-0.15	0.22	0.81	0.042	0.4
1115-1145, 26 June	-19.5	-0.15	0.24	1.00	0.053	0.6
1530-1600, 25 June	-19.6	-0.15	0.23	0.93	0.049	0.5
1000-1030, 27 June	-22.3	-0.13	0.26	1.10	0.059	0.7
1130-1200, 26 June	-22.8	-0.12	0.25	0.98	0.049	0.6
1130-1200, 25 June	-23.6	-0.12	0.33	1.25	0.117	0.5
1700-1730, 20 June	-36.5	-0.07	0.21	0.88	0.019	1.1
1025-1055, 26 June	-37.2	-0.07	0.29	0.87	0.051	0.4

250

251 **b. Spatial and temporal evolution of surface- and air-temperatures and**
252 **comparison to similarity functions**

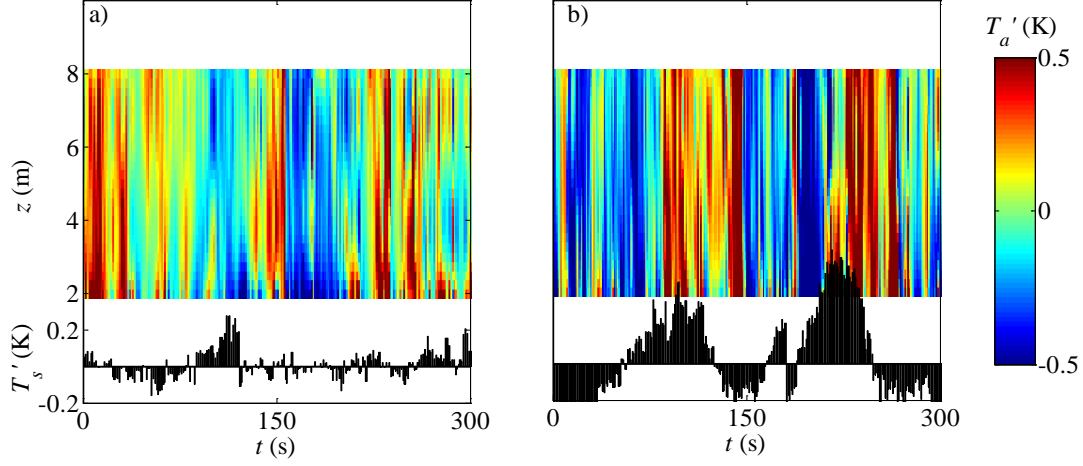
253 We have chosen the time periods with $L = -10.2$ m and -19.5 m to illustrate stability
254 dependence of surface-temperature and air turbulence data, as they are representative of more
255 unstable and less unstable conditions in our dataset with different wind-directions (177° for $L = -10.2$
256 m and 91° for $L = -19.5$ m). Structures in the spatial surface-temperature fluctuation field are aligned
257 with the wind-direction (Fig. 3) demonstrating that the observed surface-temperature structures are
258 not an artefact of surface heterogeneity or topography (also since temporal averages have been
259 removed as in Eq. 1). With time these surface-temperature structures grow, merge with each other,
260 and move along with the airflow (see supplementary material for animations).



262

263 Figure 3. Snapshots of surface-temperature fluctuations for $L =$ a) -10.2 m at 27 June 0838 UTC, and
 264 b) -19.5 m at 26 June 1124 UTC. Arrow lines represent 1-s averaged wind vectors (scaled to the
 265 distance covered in 25 sec) at 8 m (black solid), 5 m (black dashed), 3 m (white solid) and 2 m (white
 266 dashed) a.g.l. at the measurement location (white circle) respectively. The thick white line represents
 267 data excluded due to the road.

268 The temporal evolutions of surface-temperature and air-temperature fluctuations at different
 269 heights are then compared in Fig. 4. The surface-temperature is the average across the scalar footprint
 270 (Eqs. 3) of the 2-m CSAT with a cut-off of 10% of the maximum value of the scalar footprint
 271 function. Fig. 4 shows that air-temperature and surface-temperature are highly cross-correlated and
 272 air-temperature lags surface-temperature since the footprint is upstream: when the surface is cold the
 273 air cools and when the surface is warm the air warms. Also, the air-temperature at a lower altitude
 274 shows more small-scale fluctuations compared to the surface-temperature. This is due to the fact that
 275 the surface-temperature is spatially averaged across the footprint; and not as affected by the small-
 276 scale events as air-temperature, since the former has larger thermal inertia compared to the later.
 277 Comparing Figs. 4a and 4b reveals that both surface-temperature and air-temperature show more
 278 small-scale fluctuations as the boundary layer becomes more unstable. Similar results are obtained for
 279 all other stationary conditions.



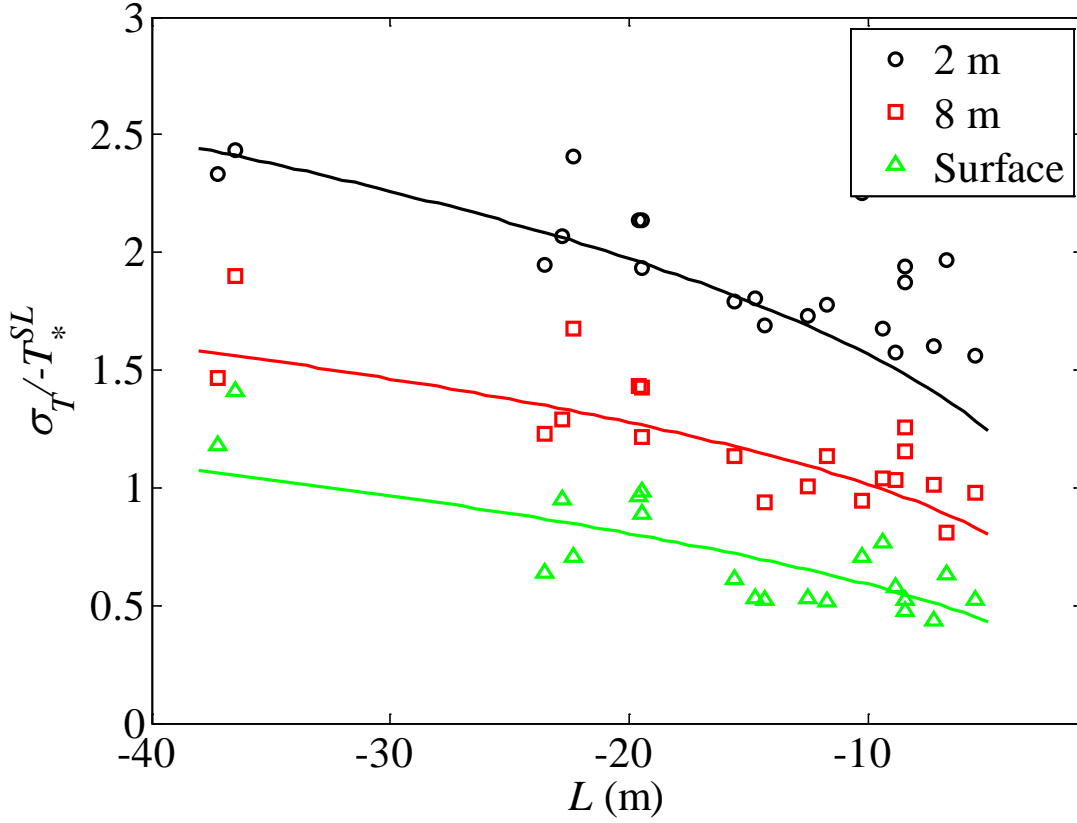
280

281 Figure 4. Time series of air-temperature (colour bar) and footprint-averaged surface-temperature (bar
 282 plot) for $L =$ a) -10.2 m at 27 June 0833 – 0838 UTC and b) -19.5 m at 26 June 1122 – 1127 UTC.
 283 Air-temperatures were vertically interpolated using spline interpolation. The footprint is the area with
 284 greater than 10% of the maximum value of the scalar footprint function of the 2-m CSAT.

285 Figure 5 shows temperature standard deviations normalized by the surface-layer temperature
 286 scale, T_*^{SL} , for all stationary periods. Normalized σ_{T_a} for 2 m and 8 m a.g.l. decrease with increasing
 287 height and stability closely following the surface-layer similarity theory,
 288 $\sigma_{T_a}/T_*^{SL} = -0.95(-z/L)^{-1/3}$ (Wyngaard et al., 1971). σ_{T_s} is smaller than σ_{T_a} at 8 m a.g.l. and
 289 satisfies $\sigma_{T_s}/T_*^{SL} = -0.36(-\zeta)^{-0.39}$.

290 DNS of the solid-fluid coupled turbulent heat transfer by Tiselj et al. (2001) showed that σ_{T_s}
 291 depends on the solid thickness and the thermal properties of solid and fluid as in the thermal activity
 292 ratio, $TAR = \frac{k_f}{k_s} \sqrt{\frac{\alpha_s}{\alpha_f}}$, where k and α are the thermal conductivity and thermal diffusivity of the fluid
 293 (subscript “ f ”) and the solid (subscript “ s ”). They found that a fluid-solid combination with low TAR
 294 does not allow imprints of fluid-temperature fluctuations on the solid surface. Balick et al. (2003) also
 295 derived a similar parameter for a coupled land-atmosphere heat transfer model. For our measurement
 296 site, one can assume the fluid-solid coupled heat transport to occur between air and homogeneous clay
 297 soil, or between air and grass leaves or a combination of both. Assuming $k_f = 0.025 \text{ W m}^{-1} \text{ K}^{-1}$ and $\alpha_f =$
 298 $20 \text{ mm}^2 \text{ s}^{-1}$, for homogeneous clay soil with 40% volumetric water content $TAR = 0.0044$ and for grass
 299 leaves with 1000 leaves m^{-2} and a weight of 10^{-3} kg per leaf (i.e. $k_s = 0.38 \text{ W m}^{-1} \text{ K}^{-1}$ and $\alpha_s = 19.62$
 300 $\text{mm}^2 \text{ s}^{-1}$, Jayalakshmy and Philip (2010)) $TAR = 0.07$. Under these conditions according to Tiselj et al.
 301 (2001) σ_{T_s} would be less than 1% for soil and about 10% for grass of its iso-flux counterpart, which
 302 corresponds to $TAR \rightarrow \infty$. Thus the air-grass leaf coupled heat transport mechanism better fits our
 303 data, as Tiselj et al. (2001) and Hunt et al. (2003) reported non-dimensional surface-temperature

304 standard deviation of 2 when temperature is modelled as passive scalar (normalized by $\frac{H}{\rho_a c_{p,a} u_*}$) and
 305 about 3 when wind shear is absent (normalized by $\frac{H}{\rho_a c_{p,a} w_*}$) for their corresponding DNSs,
 306 respectively. However, DNS results may not apply to the field measurements, as in them the Reynolds
 307 number was low, different strength of stability was used and transport of water vapour was neglected.



308

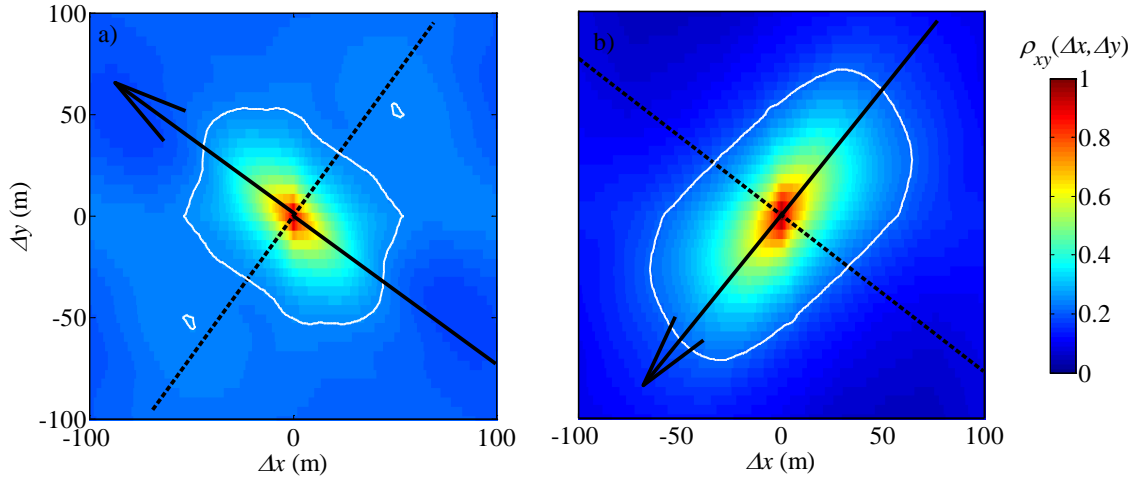
309 Figure 5. Normalized variances of surface-temperature and air-temperature as a function of L . The
 310 markers are measurements for the periods in Table 1, the black and red solid lines are fitted according
 311 to the surface-layer similarity theory $\frac{\sigma_{T^a}}{T_*^{SL}} = -0.95(-z/L)^{-1/3}$ and the green line is the fitted to
 312 the surface-temperature standard deviation: $\frac{\sigma_{T^s}}{-T_*^{SL}} = 0.36(-\zeta)^{-0.39}$.

313 c. Spatial scale of surface-temperature structures

314 The spatial scale of surface-temperature structures (as seen in Fig. 3) can be investigated by
 315 considering the spatial correlation for each image using

$$316 \quad \rho_{xy}(\Delta x, \Delta y, t) = \frac{T_s'(x, y, t) T_s'(x + \Delta x, y + \Delta y, t)}{\sigma_{T_s}^2}, \quad (5)$$

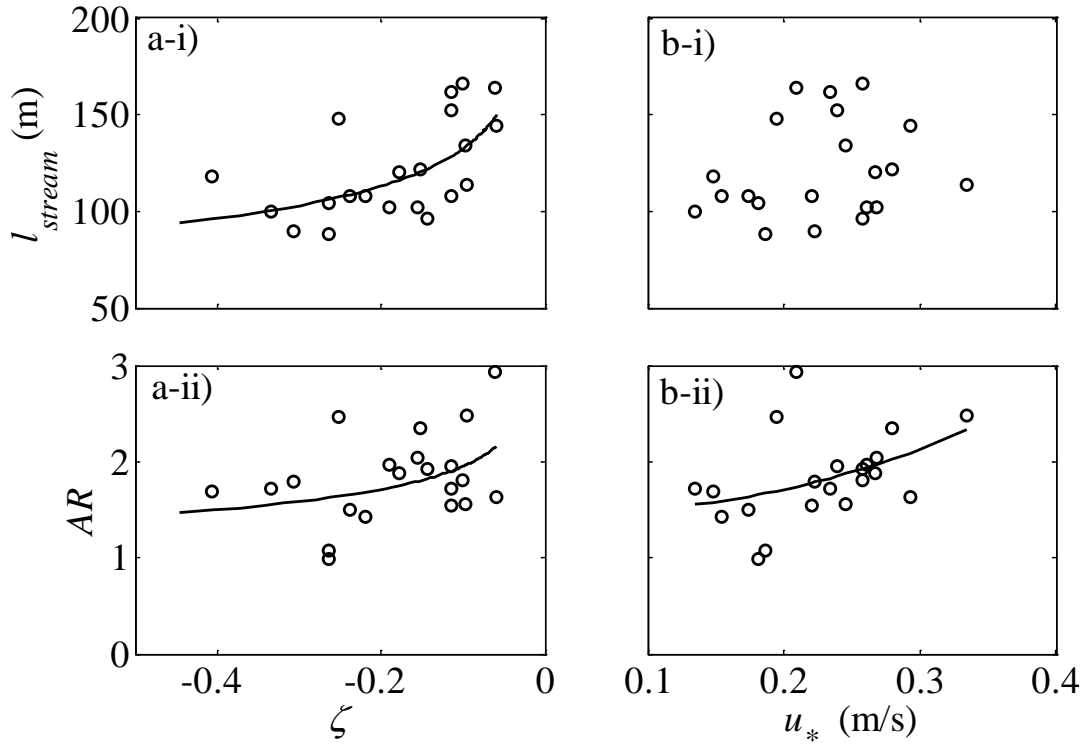
317 where the overbar indicates a spatial average. Figure 6 shows the temporal average of the spatial
 318 correlation of the surface-temperature structures ($\langle \overline{\rho_{xy}(\Delta x, \Delta y, t)} \rangle$) for $L =$ (a) -10.2 m, and (b) -19.5
 319 m. The surface-temperature correlation structures are shaped as ellipsoids with the major axis aligned
 320 with the streamwise direction.



321
 322 Figure 6. Mean spatial correlation of surface-temperature for $L =$ (a) -10.2 m, and (b) -19.5 m (in
 323 the camera coordinate system). The solid and broken black lines indicate averaged streamwise and
 324 spanwise directions over 2, 3, 5 and 8 m a.g.l., respectively. The white contour line indicates a
 325 correlation of 0.25.

326 The spatial properties of coherent structures in a boundary layer flow depend on shear and
 327 buoyancy. For a shear-dominated boundary layer, the structures become elongated in the wind-
 328 direction and streaky, whereas for a buoyancy-dominated boundary layer, they become more circular.
 329 We consider u_* as a measure of shear and ζ as a relative measure of buoyancy to study their effect on
 330 the surface-temperature structures. Figure 7 shows (i) the streamwise correlation length (l_{stream}), and
 331 (ii) the aspect ratio ($AR = l_{stream}/l_{span}$, where l_{span} is the spanwise correlation length) against ζ and u_* for
 332 all stationary periods. The correlation length is defined as twice the distance from the centre where the
 333 correlation becomes 0.25 in the streamwise and spanwise directions (Fig. 6). Though the quantitative
 334 values of the streamwise and spanwise lengths will depend on the chosen cut-off correlation, the
 335 qualitative behaviour of the streamwise and spanwise lengths with stability and friction velocity are
 336 independent of the chosen correlation cut-off value. The spatial scales of surface-temperature
 337 structures will also depend on the averaging period, as the camera field-of-view could not capture the
 338 largest possible structure in CBL. A 30-min averaging period resulted in structures 20 to 40% larger
 339 than those computed using a 5-min averaging period. With increasing stability the structures become

340 streakier. Thus AR is close to unity for the more unstable cases and larger than unity for the less
 341 unstable cases. Hommema and Adrian (2003) and Li and Bou-Zeid (2011) also reported that as the
 342 boundary layer becomes more unstable, the dominant coherent structures in the surface-layer change
 343 from long streaky structures due to hairpin packets to surface-layer plumes. l_{stream} does not show any
 344 recognizable trend against u_* , but AR increases from 1.5 for small u_* to more than 2 for larger u_* .
 345 Wilczak and Tillman (1980) reported similar streamwise sizes of coherent structures based on the
 346 time traces of air-temperature at 4 m a.g.l..



347

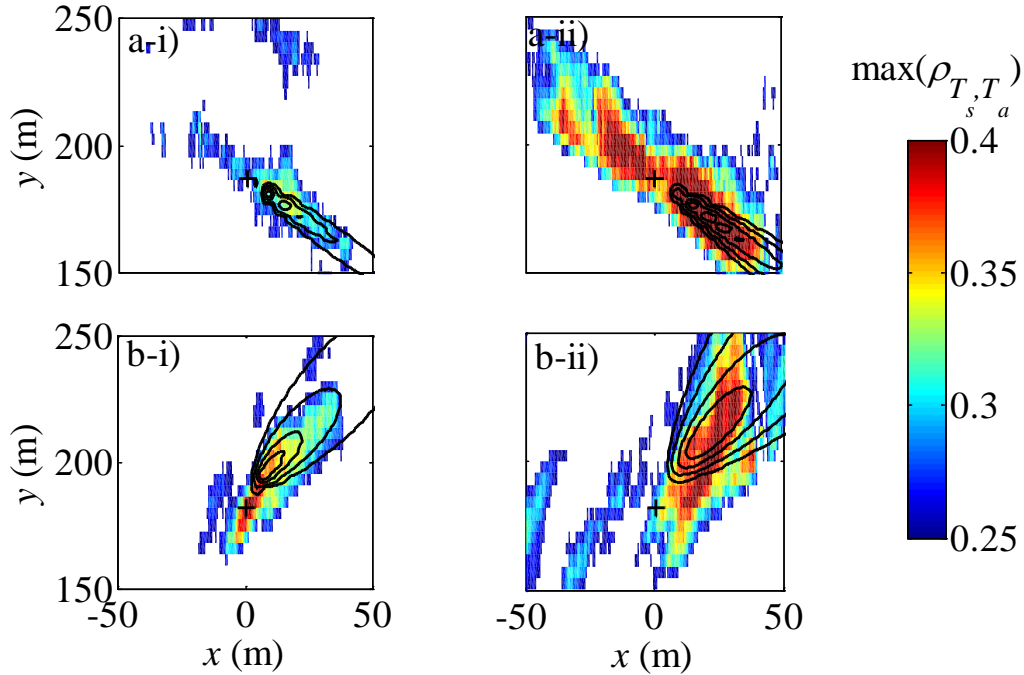
348 Figure 7. (i) Streamwise correlation length l_{stream} , and (ii) aspect ratio AR of the mean surface-
 349 temperature structure with (a) ζ and (b) u_* . Markers represent the measurements and solid lines
 350 represent fits: $l_{stream} = 78.03(-\zeta)^{-0.23}$, $AR = 1.26(-\zeta)^{-0.19}$, $AR = 11.43u_*^2 - 1.5u_* + 1.55$ with
 351 48.6%, 28.0% and 27.7% coefficient of determination respectively. No trend was observed and no
 352 line was fitted for b-i.

353 d. Surface- and air-temperature correlation

354 Since the footprint-averaged surface-temperature is correlated with air-temperature (Fig. 4),
 355 spatial maps of cross-correlation between surface-temperature and air-temperature were generated
 356 using

$$357 \quad \rho_{T_s, T_a}(x, y, \Delta t) = \frac{\langle T'_s(x, y, t) T'_a(x_0, y_0, t + \Delta t) \rangle}{\sigma_{T_s} \sigma_{T_a}}, \quad (6)$$

358 where x_o and y_o are the coordinates of the sonic tower and the two vectors are lagged by up to $\Delta t = 60$
 359 sec. To reduce noise in the cross-correlation maps, an ensemble average of three cross-correlation
 360 maps for each 10-min interval in a 30 min-stationary period was computed. Spatial maps of maximum
 361 cross-correlations between surface-temperature and air-temperature at (i) 2 m, and (ii) 8 m a.g.l. are
 362 shown in Fig. 8. The region of maximum cross-correlation between surface-temperature and air-
 363 temperature is elongated in the wind direction. The upwind correlation region and the scalar footprint
 364 function show significant overlap (however, note the footprint obviously only extends upwind while
 365 the correlation region extends upwind and downwind). Specifically, the cross-wind spread of the
 366 maximum correlation region is similar to that of the footprint function (Eq. 3c). The maximum
 367 correlation coefficient, size of the correlation region, and the footprint increase when the 8-m air-
 368 temperature is correlated with the surface-temperature. Similar trends are also observed for the other
 369 stationary periods.



370

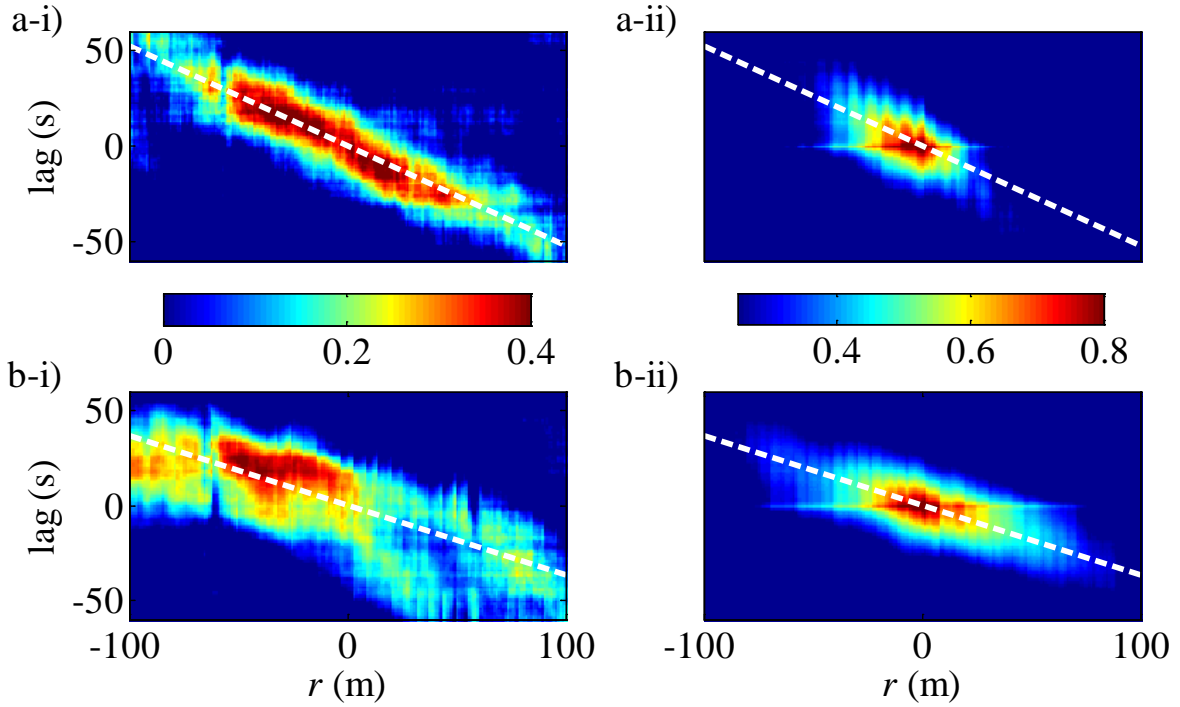
371 Figure 8. 30-minute maximum cross-correlation between surface-temperature and air-temperature at
 372 (i) 2 m and (ii) 8 m with scalar footprint model (Eq. 3, black contours) for $L =$ (a) -10.2 m, and (b)
 373 -19.5 m. White pixels represent surface- and air-temperature correlation less than 0.25 or
 374 unreasonable lags (absolute lag greater than 60 s). The black contour lines represent 10, 25, 50 and
 375 75% of the maximum of scalar footprint function. The black '+' sign marks the location of the sonic
 376 tower ($x_o = 0.4$ m and $y_o = 185$ m).

377 Along the wind-direction cross-correlations between the air-temperature at 8 m a.g.l. and the
 378 lagged surface-temperature (Figs. 8-ii) are then plotted in Figs. 9-i. Here, positive r indicates the
 379 downwind direction and positive lags indicate that the surface is preceding the air and vice versa. The
 380 largest cross-correlations for the upwind (downwind) correlation region occur at a positive (negative)
 381 lag (shown in Figs. 9-i). Thus the upwind surface-temperature is affecting the air-temperature at the
 382 measurement location and the air-temperature at the measurement location is affecting the downwind
 383 surface-temperature, consistent with Garai and Kleissl (2011). Cross-correlations between *surface-*
 384 *temperatures* along the wind-direction are shown in Figs. 9-ii as calculated using

$$385 \quad \rho_{T_s, T_s}(r, \Delta t; x_*, y_*) = \frac{\langle T_s'(x_* + r \cos \theta, y_* + r \sin \theta, t + \Delta t) T_s'(x_*, y_*, t) \rangle}{\sigma_{T_s}^2}, \quad (7)$$

386 where x_* , y_* , and θ are arbitrary coordinates in the image and wind-direction. To reduce the noise of
 387 the cross-correlation between surface-temperatures, ensemble averages from 15 different (x_*, y_*)
 388 positions were computed. Note the distinction between these cross-correlations versus the spatial
 389 correlations $\rho_{xy}(\Delta x, \Delta y, t)$ described in Section 3c; the former ‘tracks’ surface-temperature structures
 390 by co-varying space (r) and time (Δt), while the latter correlates structures that are not time shifted
 391 across space. Therefore, $\rho_{xy}(\Delta x, \Delta y, t)$ represents the typical spatial extent of surface-temperature
 392 structures at a given time and $\rho_{T_s, T_s}(r, \Delta t; x_*, y_*)$ represents the spatio-temporal region of influence of
 393 a given structure. If a structure remained unchanged as it moves across the image, $\rho_{T_s, T_s}(r, \Delta t; x_*, y_*)$
 394 would be large.

395 For the correlations between surface-temperatures, a positive lag indicates that the upwind
 396 surface-temperature is preceded by downwind surface-temperature. The cross-correlations between
 397 the surface-temperatures in Figs. 9-ii are larger compared to the cross-correlations between air-
 398 temperature and surface-temperature in Fig. 9-i as the latter is calculated between two different
 399 variables and heights. Since the spatial extent of the high correlation region between the air-
 400 temperature and surface-temperature depends on the air-temperature measurement height, it is not
 401 useful to compare quantitatively the spatial extents of the high correlation regions for air-temperature
 402 and surface-temperature with that for the surface-temperatures at a given stability. Qualitatively, as
 403 the stability of the boundary layer increases, the spatial extent of the high correlation region between
 404 air-temperature and surface-temperature; and between surface-temperatures increases. A less unstable
 405 boundary layer will contain longer turbulence structures which is manifested in the larger footprints in
 406 Fig. 9-i. The cross-correlations between air-temperature and surface-temperature; and between
 407 surface-temperatures allow tracking the advection speed of the structures responsible for land-
 408 atmosphere exchange.



409

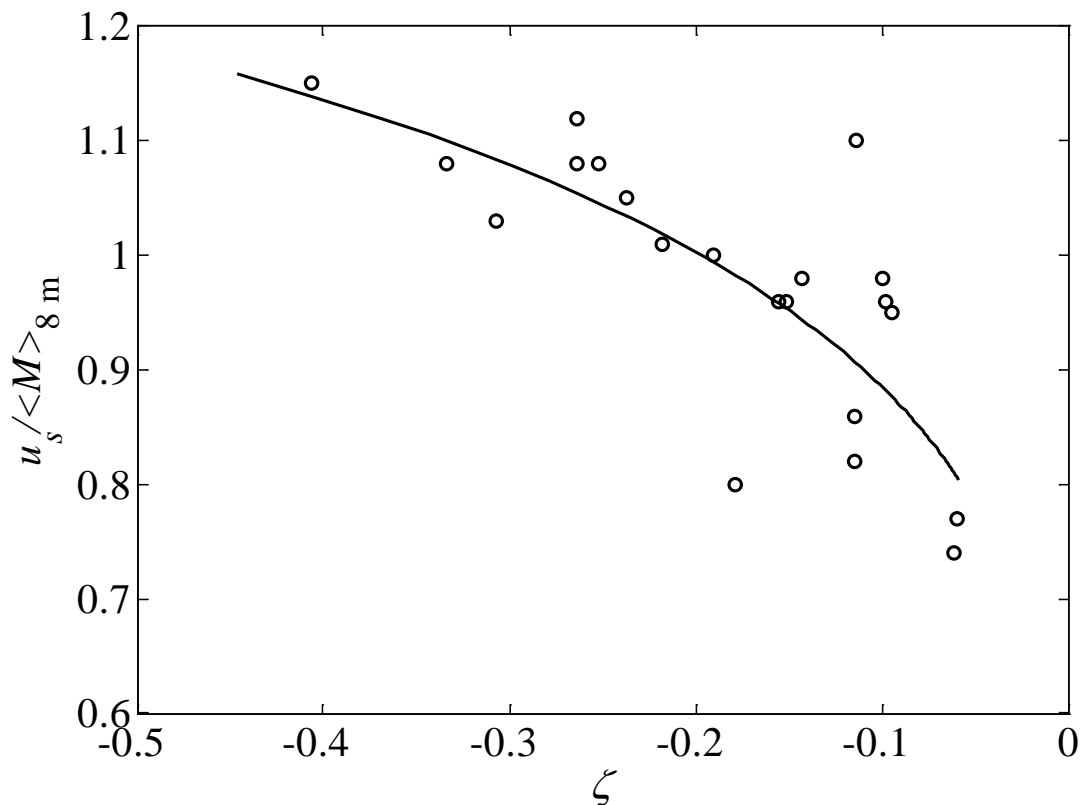
410 Figure 9. Left panels: Cross-correlation between air-temperature at 8 m with surface-temperature
 411 along the 8-m wind-direction at different lags. Right panels: Cross-correlation amongst surface-
 412 temperature along the 8-m wind-direction at different lags. (a) $L = -10.2$ m, and (b) $L = -19.5$ m.
 413 The white dashed line represents the slope of the cross-correlation area.

414 e. Advection speed of the surface-temperature structures

415 The cross-correlation surfaces between air-temperature and surface-temperature; and between
 416 surface-temperatures in Fig. 9 show similar slopes for a given stationary period, which is further
 417 evidence for the advective nature of the surface-temperature coherent structures. The slope of the
 418 cross-correlation indicates the advection speed u_s of the surface-temperature structures (or rather the
 419 turbulent coherent structures that leave an imprint on the surface) along the wind-direction. The
 420 estimated advection speeds for all stationary periods are plotted in Fig. 10. The scatter in the plot is
 421 mostly due to the uncertainty in estimating the slope; for some wind-directions the high correlation
 422 region is discontinuous (as seen in Figure 8b-ii, 9b-i) due to surface heterogeneity. The advection
 423 speeds are similar to the wind-speed at 8 m a.g.l. with a decreasing trend in less unstable conditions.

424 Wilczak and Tillman (1980) also reported that the speeds of surface-layer plumes are greater
 425 than the wind speed at 4 m a.g.l. with a small decreasing trend with stability. As the surface-layer
 426 becomes less unstable, the strength of buoyant production decreases compared to shear production,
 427 resulting in less turbulent mixing. This causes a larger vertical gradient of horizontal wind-speed in
 428 the upper part of the surface-layer and also a smaller effective plume height. The advection speed, i.e.

429 the mean wind-speed over the height of the surface-layer plume, should be identical to u_s of the
 430 surface-temperature coherent structures. Thus, with increase in the stability of the boundary layer u_s
 431 decreases compared to the wind-speed at a sufficiently large altitude (e.g. 8 m a.g.l. in this case). Also
 432 as seen in Figs. 2-c, except for 25 June the mixed-layer wind-speed is similar to the wind-speed at 8 m
 433 a.g.l. Consequently, one can conclude that u_s is similar to the mixed-layer wind-speed. This is
 434 consistent with Katul et al. (1998) and Renno et al. (2004), who in the absence of thermal imagery,
 435 resorted to more elaborate spectral analysis to suggest that surface-temperature structures are caused
 436 by mixed-layer turbulence.



437
 438 Figure 10. Advection velocity of the surface-temperature structures (determined from Fig. 9) versus
 439 the 8-m wind-speed as a function of ζ . Markers represent the measurements and the solid line
 440 represents the fitted equation $u_s / \langle M \rangle_{8m} = 1.34(-\zeta)^{0.18}$ with 57.1% coefficient of determination.

441 f. Conditional averaging of ejection events

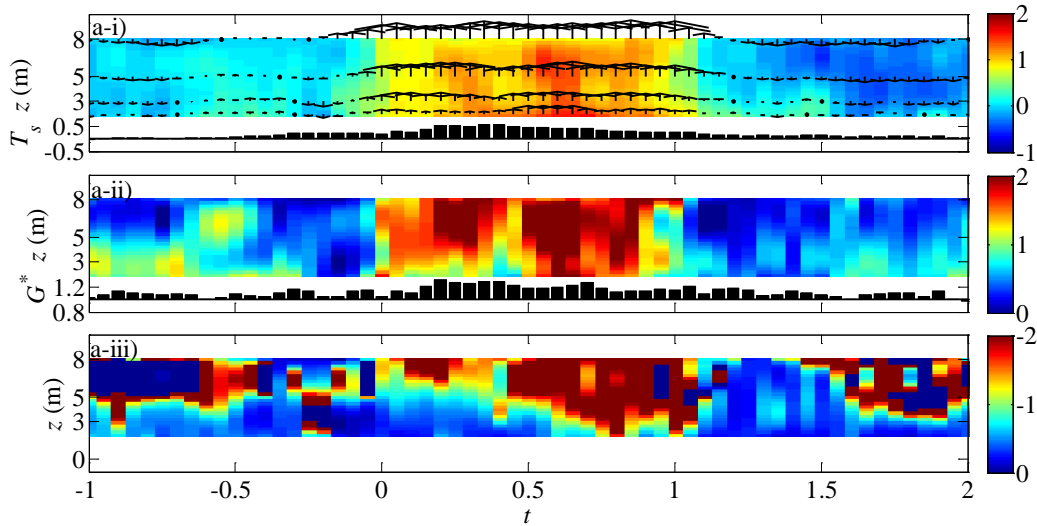
442 To study the coupling between surface-temperature and near surface coherent structures in
 443 more detail, conditional averaging was employed. Events are classified as strong ejection events if
 444 $w'T_a'_{8m} > 0.5\langle w'T_a' \rangle_{8m}$, w' is positive, and the minimum duration of the event is 3 s. Also, if two
 445 consecutive events are separated by less than 5 s, they are merged into a single event. The events are
 446 then verified by visual inspection of the time series to avoid false identification. These criteria result

447 in 20 to 30 ejection events per stationary period with time scales ranging from 3 s to 45 s. Since the
448 duration of each ejection event is different, time was normalized by the individual ejection time scale
449 such that $t = 0$ and 1 indicates the start and end of the ejection event at 8 m a.g.l. respectively.

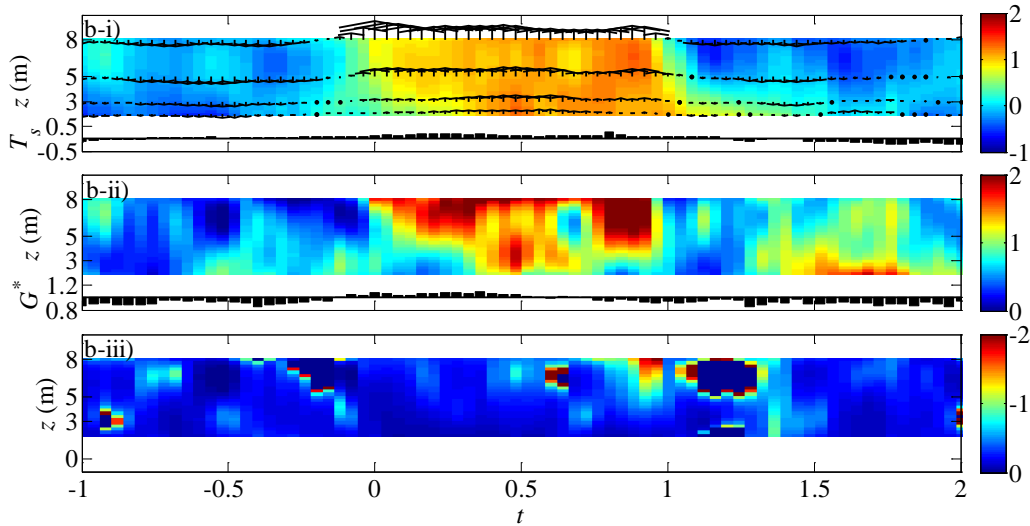
450 The events cover around 20 to 25% of each 30-min stationary period, but are responsible for
451 60 to 70% of the sensible heat-flux. The ejection event is initiated by surface heating (Fig. 11-i). Since
452 net radiation is nearly constant during the short duration of the event, the increase in ground heat-flux
453 associated with surface heating has to be balanced by decreases in the convective fluxes. Thus before
454 the ejection event, $w'T_a'$ is small. During the ejection event (Fig. 11-i) the warm air rises due to
455 buoyancy, forming a surface-layer plume. The majority of the vertical heat-flux occurs at the end of
456 the ejection event (Fig. 11-ii) and buoyant production increases compared to shear production (Fig.
457 11-iii). After the ejection event, a downward flow of cold air occurs as a sweep event. The large
458 convective heat-flux during the ejection leads to cooling of the surface and as a result the ground heat-
459 flux decreases until the end of the sweep event. Also, note that though air-temperature shows a ramp-
460 like pattern (air-temperature remains almost constant during the sweep, gradually increases during the
461 sweep to ejection transition, attains maximum at the ejection and drops sharply during the ejection to
462 sweep transition), the change in surface-temperature is smoother (gradual increase and decrease
463 during sweep to ejection and to sweep events). This might be attributed to the higher thermal inertia
464 of the surface compared to the air, so that small scale variations average out over the surface.

465 Though air-temperature and surface-temperature follow similar trends, there is a time lag; the
466 surface-temperature reaches its maximum before the air-temperature and its minimum after the air-
467 temperature consistent with Garai & Kleissl (2011). Also, from Figs. 11-i, it is evident that the plumes
468 are slightly tilted due to wind shear. Since the shear production decreases more rapidly with height
469 than buoyant production, the magnitude of Ri_f increases with height (Figs. 11-iii). Also, the magnitude
470 of Ri_f during the ejection event decreases with increasing stability of the boundary layer. Similar
471 results are obtained for the other stationary periods.

472 Although the magnitude of G depends on the thermal properties of the ground, the ground
473 heat-flux normalized by the mean, $G^* = G/\langle G \rangle$, is independent of ground thermal properties as the
474 ground conduction model is linear. Figs. 11-ii show that the ejection and sweep events cause
475 variations of up to 0.3 times the mean ground heat-flux.



476



477

478 Figure 11. Conditional average of ejection events occurring for $L =$ (a) -10.2 m, and (b) -19.5 m. (i)
 479 air-temperature (colour), and surface-temperature (bars), both normalized by $-T_*^{SL}$. Vertical velocity
 480 vectors are overlayed (the largest vectors correspond to 0.4 m s^{-1}). To convert surface-temperature to a
 481 time series, Taylor's frozen turbulence hypothesis was applied using the advection speed of surface-
 482 temperature structures (Fig. 9). (ii) $w'T_a'$ normalized by $\langle w'T_a' \rangle_{2m}$ (colour) and modelled ground
 483 heat-flux normalized by mean ground heat-flux (G^* , bars). (iii) Ri_f . The time axes are normalized such
 484 that $t = 0$ and 1 correspond to the start and the end of the ejection event at 8 m a.g.l. , respectively.

485 Note that the surface-temperature is not from the footprint of the air-temperature, but rather the
 486 temperature directly below the air-temperature measurements.

487 4. Discussion and conclusion

488 Coupled land-atmosphere heat transfer was examined using lower surface-layer eddy-
 489 covariance measurements and IR surface-temperature imagery for a range of unstable conditions in

490 the CBL. The sequential IR images of surface-temperature show that temperature patterns in the
491 surface grow, combine with each other and move along with the wind. These surface-temperature
492 patterns can be interpreted to be the imprints of turbulent coherent structures on the surface in a CBL
493 (Derksen, 1974; Schols et al. 1985; Paw U et al. 1992; Katul et al. 1998; Balick et al. 2003; Ballard et
494 al. 2004; Renno et al. 2004; Vogt, 2008; Christen and Voogt, 2009, 2010; Christen et al. 2011; Garai
495 and Kleissl, 2011). When the surface-temperature standard deviation is compared with the air-
496 temperature standard deviation, this follows a similar trend with respect to stability and the former is
497 smaller in magnitude than the latter at 8 m a.g.l. The normalized σ_{TS} gives a similar power-law
498 exponent (0.39) compared to surface-layer similarity theory (Wyngaard et al., 1971); the coefficient
499 of proportionality differs significantly (for our data, 0.36), but it should depend on the surface thermal
500 property (Tiselj et al., 2001; Balick et al., 2003). Different σ_{TS} over different surfaces (σ_{TS} over
501 metallic roofs > lawns > roads > building walls) were also reported by Christen et al. (2012) for an
502 urban measurement site.

503 Cross-correlating surface-temperature and air-temperature, the maximum correlation region is
504 aligned with the wind-direction. The cross-wind span of the correlation region increases with the
505 standard deviation of the wind-direction. The upwind correlation region corresponds well to the scalar
506 footprint formulated from the model by Hsieh et al. (2000). The lag associated with the maximum
507 correlation reveals that the upwind surface-temperature fluctuations affect the air-temperature
508 fluctuations at the measurement tower and the air-temperature fluctuations at the measurement tower
509 affect the downwind surface-temperature fluctuations. This indicates that vertically coherent
510 structures advect cold and warm fluid downwind and these structures leave a temperature footprint on
511 the surface. The correlation between footprint-averaged surface-temperature with air-temperature
512 increases from 2 m to 8 m. All these observations point to the surface-temperature fluctuations being
513 caused by turbulent coherent structures in the atmospheric boundary layer.

514 The mean streamwise size of the surface-temperature structures (or rather the turbulent
515 coherent structures that leave an imprint on the surface) decreases with ζ . The aspect ratio (AR) of the
516 structures increases with both u_* and ζ . Wilczak and Tillman (1980) also reported similar sizes of
517 coherent structures and their advection speed in the CBL by considering the time trace of air-
518 temperature at 4 m a.g.l.. These findings further substantiate that the surface-temperature patterns
519 reflect common properties of turbulent coherent structures in the boundary layer. More unstable flows
520 cause more circular and shorter coherent structures while more neutral flows give rise to longer,
521 streaky patterns, consistent with the observations of Hommema and Adrian (2003) and Li and Bou-
522 Zeid (2011). Katul et al. (2011) related the change in the coherent structures with instability to the
523 Businger-Dyer relationships.

524 The advection speed of the structures was of the order of the wind-speed at 8 m a.g.l. and it
525 decreased with stability. The mixed-layer wind-speed was almost the same as the wind-speed at 8 m
526 a.g.l.. Similar results were reported by Christen and Voogt (2009, 2010) and Garai and Kleissl (2011).
527 Katul et al. (1998) and Renno et al. (2004) inferred that high frequency surface-temperature
528 fluctuations were caused by mixed-layer turbulence.

529 The surface-temperature coherent structures are finally interpreted in the context of the
530 surface renewal method. While the Lagrangian concept of the surface renewal method cannot be
531 conclusively demonstrated in the Eulerian measurement framework, the observations give rise to the
532 following interaction between coherent structures and the surface. During the sweep event, a cold air
533 parcel descends and the surface cools due to enhanced temperature differences and heat transfer
534 between surface and air. The cooler surface results in a smaller ground heat-flux during this time
535 (Figs. 11-i and ii; $t > 1$ or $-1 < t < -0.5$). As the air parcel remains in contact with the surface it
536 warms gradually, reducing heat transfer between the surface and the air. The ground heat-flux
537 increases during this time. Thus, the surface starts to warm (Figs. 11-i and ii; $-0.5 < t < 0$). As the air
538 parcel warms up, it gains buoyancy (Figs. 11-iii). With sufficient buoyancy (and possibly assisted by
539 mixed-layer turbulence) the air parcel ascends in an ejection event. During the initial period of the
540 ejection event, the ground heat-flux reaches a maximum (Figs. 11-i; $0 < t < 0.5$). As the ejection event
541 continues greater heat transfer occurs between the surface and the air (Figs. 11-ii; $0 < t < 0.5$).
542 Afterwards the surface starts to cool and the ground heat-flux starts to decrease (Figs. 11-ii; $t > 0.5$).

543 In Garai and Kleissl (2011), we also analyzed surface-temperature structures during different
544 phases of the surface renewal cycle. In this study, with the larger camera field-of-view and availability
545 of air-temperature at different heights, we have successfully visualized surface renewal events both in
546 the surface-layer and on the surface. However, due to the larger camera field-of-view in this study, a
547 single image contains several surface renewal events at different stages (Fig. 3). Thus the size of the
548 surface-temperature structure for each individual surface renewal event is averaged out when spatial
549 correlation within an image is considered (Section 3c). While it cannot be demonstrated in this study,
550 we expect the temporal evolution of the structure size to be similar, as found in Garai and Kleissl
551 (2011): during the ejection event there will be a large warm surface-temperature structure, during the
552 sweep event there will be a large cold surface-temperature structure, at the transition from ejection to
553 sweep there will be small patches of cold surface-temperature structures, and at the transition from
554 sweep to ejection there will be small patches of warm surface-temperature structures. These surface-
555 temperature structures grow, combine with each other and move along the higher altitude wind.
556 Strong sweep events are followed by ejection events and the heat transfer mechanism repeats itself.
557 We observed that the surface reaches maximum temperature before the air and minimum temperature
558 after the air. The majority of heat transport occurs during the ejection event (about 60 to 70% of the

559 total sensible heat-flux), which also causes ground heat-flux variations (about 30% of the mean
560 ground heat-flux) through the surface energy budget.

561 These surface-temperature coherent structures with spatial scales of several hundred metres
562 and temperature variations of 0.5 – 1 K, depending on the boundary layer instability, can reduce the
563 accuracy of different remote sensing applications. The turbulence-induced surface-temperature
564 variations should also be accounted for in numerical models, since they produce considerable surface
565 energy budget anomalies.

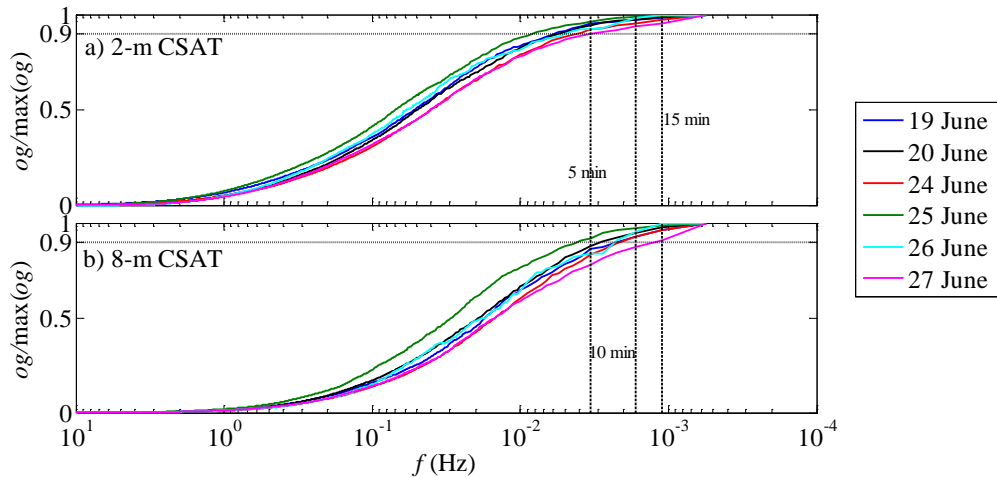
566

567 **Acknowledgements:** We thank (i) Daniel Alexander from University of Utah, USA; Dr. Marie
568 Lothon, Dr. Fabienne Lohou, Solene Derrien from Laboratoire d'Aérodynamique, Université de Toulouse,
569 France; Dr. Arnold Moene, Dr. Oscar Hartogensis, Anneke Van de Boer from Wageningen
570 University, Netherlands for field assistance, data sharing and discussion; (ii) Peter Cottle and Anders
571 Nottrott from University of California, San Diego for pre-experimental laboratory assistance and
572 discussion about the data analysis respectively; (iii) BLLAST organizers for their hospitality during
573 the experiment; (iv) funding from a NASA New Investigator Program award for AG and JK, and from
574 INSU-CNRS (Institut National des Sciences de l'Univers, Centre national de la Recherche
575 Scientifique, LEFE-IDAO program), Météo-France, Observatoire Midi-Pyrénées (University of
576 Toulouse), EUFAR (EUropean Facility for Airborne Research) and COST ES0802 (European
577 Cooperation in the field of Scientific and Technical) for the BLLAST field experiment.

578

579 Appendix

580 The ogive function can be employed to estimate the sufficient averaging period for
581 calculation of turbulent fluxes using the eddy-covariance method. Ogive ($og_{w,X}(f_o)$) is a cumulative
582 integral of the cospectrum, $Co_{w,X}$, of a variable, X , with vertical velocity, w , starting with the highest
583 frequency, f , $og_{w,X}(f_o) = \int_{\infty}^{f_o} Co_{w,X}(f)df$. Ideally the ogive function increases during the integration
584 from high frequency to small frequency, until reaching a constant value. Hence the period
585 corresponding to the frequency at which the ogive reaches the constant value is considered to be
586 sufficient to capture the largest turbulence scales. To improve the statistical significance and minimize
587 the effect of diurnal cycles, twenty six 30-min segments for each clear days corresponding to 0600 –
588 1900 UTC were used. It was found that a 5-min averaging period accounts for 90% and 85% of the
589 maximum value of ogive for 2-m and 8-m CSATs respectively for the sensible heat-flux (Fig. 12)
590 and the momentum-flux (not shown). Thus an averaging period of 5-min was selected.



591

592 Figure 12. The normalized ogive by its maximum value for heat-flux calculation at 2-m and 8-m
 593 CSAT of all the clear days.

594

595 **References**

596 Balick LK, Jeffery CA, Henderson B (2003) Turbulence induced spatial variation of surface
 597 temperature in high resolution thermal IR satellite imagery. Proc SPIE 4879:221-230.

598 Ballard JR, Smith JA, Koenig GG (2004) Towards a high temporal frequency grass canopy
 599 thermal IR model for background signatures. Proc SPIE 5431:251-259.

600 Bastiaanssen WGM, Menenti M, Feddes RA, Holstag AAM (1998a) A remote sensing
 601 surface energy balance algorithm for land (SEBAL). 1. Formulation. J Hydrol 212-
 602 213: 198-212.

603 Bastiaanssen WGM, Pelgrum H, Wang J, Ma J, Moreno JF, Roerink GJ, van der Wal T
 604 (1998b) A remote sensing surface energy balance algorithm for land (SEBAL). 2.
 605 Validation. J Hydrol 212-213:213-229.

606 Braaten DA, Shaw RH, Paw U KT (1993) Boundary-layer flow structures associated with
 607 particle reentrainment. Boundary-Layer Meteorol 65:255-272.

608 Businger JA, Wyngaard JC, Izumi Y, Bradley EF (1971) Flux profile relationships in the
 609 atmospheric surface layer. J Atmos Sci 28:181-189.

- 610 Campbell GS, Norman JM (1998) An introduction to environmental biophysics. Springer
611 Verlag, New York, USA, 286 pp.
- 612 Carslaw HS, Jaeger JC (1959) Conduction of heat in solids. Oxford University Press,
613 London, UK, 510 pp.
- 614 Castellvi F (2004) Combining surface renewal analysis and similarity theory: a new approach
615 for estimating sensible heat flux. *Water Resour Res* 40:W05201.
- 616 Castellvi F, Perez PJ, Ibanez M (2002) A method based on high-frequency temperature
617 measurements to estimate the sensible heat flu avoiding the height dependence. *Water*
618 *Resour Res* 38(6):1084.
- 619 Castellvi F, Snyder RL (2009) Combining the dissipation method and surface renewal
620 analysis to estimate scalar fluxes from the time traces over rangeland grass near Ione
621 (California). *Hydrol Process* 23:842-857.
- 622 Christen A, Meier F, Scherer D (2012) High-frequency fluctuations of surface temperatures
623 in an urban environment, *Theor Appl Climatol* 108:301-324.
- 624 Christen A, Voogt JA (2009) Linking atmospheric turbulence and surface temperature
625 fluctuations in a street canyon. Paper no. A3-6. The 7th International Conference on
626 Urban Climate, Yokohoma, Japan.
- 627 Christen A, Voogt JA (2010) Inferring turbulent exchange process in an urban street canyon
628 from high-frequency thermography. Paper no. J3A.3. 9th Symposium on the Urban
629 Environment, Keystone, Colorado, USA.
- 630 Derksen DS (1974) Thermal infrared pictures and the mapping of microclimate. *Neth J Agric*
631 *Sci* 22:119-132.
- 632 Foken T, Wimmer F, Mauder M, Thomas C, Liebethal C (2006) Some aspects of the energy
633 balance closure problem. *Atmos Chem Phys* 6:4395-4402.
- 634 Gao W, Shaw RH, Paw U KT (1989) Observation of organized structure in turbulent flow
635 within and above a forest canopy. *Boundary-Layer Meteorol* 47:349-377.
- 636 Garai A, Kleissl J (2011) Air and surface temperature coupling in the convective atmospheric
637 boundary layer. *J Atmos Sci* 68:2945-2954.

638 Gurka R, Liberzon A, Hestroni G (2004) Detecting coherent patterns in a flume by using PIV
639 and IR imaging techniques. *Exp Fluids* 37:230-236.

640 Hestroni G, Rozenblit R (1994) Heat transfer to a liquid-solid mixture in a flume. *Int J*
641 *Multiphase Flow* 20:671-689.

642 Hestroni G, Kowalewski TA, Hu B, Mosyak A (2001) Tracking of coherent thermal
643 structures on a heated wall by means of infrared thermography. *Exp Fluids* 30:286-
644 294.

645 Hommema SE, Adrian RJ (2003) Packet structure of surface eddies in the atmospheric
646 boundary layer. *Boundary-Layer Meteorol* 106:147-170.

647 Howard LN (1966) Convection at high Rayleigh number. *Proceedings of the 11th*
648 *International Congress on Applied Mechanics*, H. Görtler, Ed., Springer-Verlag,
649 1109-1115.

650 Hsieh C-I, Katul GG, Chi T (2000) An approximate analytical model for footprint estimation
651 of scalar fluxes in thermally stratified atmospheric flows. *Adv Water Resour* 23:765-
652 772.

653 Hunt JCR, Vrieling AJ, Nieuwstadt FTM, Fernando HJS (2003) The influence of the thermal
654 diffusivity of the lower boundary on eddy motion in convection. *J Fluid Mech*
655 491:183-205.

656 Jayalakshmy MS, Philip J (2010) Thermophysical properties of plant leaves and their
657 influence on the environment temperature. *Int J Thermophys* 31:2295-2304.

658 Kaimal JC, Businger JA (1970) Case studies of a convective plume and a dust devil. *J Appl*
659 *Meteorol* 9:612-620.

660 Kaimal JC, Wyngard JC, Haugen DA, Cote OR, Izumi Y (1976) Turbulence structure in the
661 convective boundary layer. *J Atmos Sci* 33:2152-2169.

662 Katul GG, Konings AG, Porporato A (2011) Mean velocity profile in a sheared and thermally
663 stratified atmospheric boundary layer. *Phys Rev Lett* 107:268502.

664 Katul GG, Schieldge J, Hsieh C-I, Vidakovic B (1998) Skin temperature perturbations
665 induced by surface layer turbulence above a grass surface. *Water Resour Res*
666 34:1265-1274.

667 Kormann R, Meixner FX (2001) An analytical footprint model for non-neutral stratification.
668 *Boundary-Layer Meteorol* 99:207-224.

669 Li D, Bou-Zeid E (2011) Coherent structures and the dissimilarity of turbulent transport of
670 momentum and scalars in the unstable atmospheric surface layer. *Boundary-Layer*
671 *Meteorol* 140:243-262.

672 Lothon M, Lohou F, Durand P, Couvreux Sr. F, Hartogensis OK, Legain D, Pardyjak E, Pino
673 D, Reuder J, Vilà Guerau de Arellano J, Alexander D, Augustin P, Bazile E,
674 Bezombes Y, Blay E, van de Boer A, Boichard JL, de Coster O, Cuxart J, Dabas A,
675 Darbieu C, Deboudt K, Delbarre H, Derrien S, Faloona I, Flament P, Fourmentin M,
676 Garai A, Gibert F, Gioli B, Graf A, Groebner J, Guichard F, Jonassen M, van de
677 Kroonenberg A, Lenschow D, Martin S, Martinez D, Mastrorillo L, Moene A, Moulin
678 E, Pietersen H, Piguet B, Pique E, Román-Cascón C, Said F, Sastre M, Seity Y,
679 Steeneveld GJ, Toscano P, Traullé O, Tzanos D, Wacker S, Yagüe C (2012) The
680 boundary layer late afternoon and sunset turbulence 2011 field experiment. Paper no.
681 14B.1. 20th Symposium on Boundary Layers and Turbulence, Boston, Massachusetts,
682 USA.

683 Oke TR (1987) *Boundary layer climates*. Methuen, London, UK, 435 pp.

684 Paw U KT, Brunet Y, Collineau S, Shaw RH, Maitani T, Qiu J, Hipps L (1992) On coherent
685 structures in turbulence above and within agricultural plant canopies. *Agric For*
686 *Meteorol* 61:55-68.

687 Paw U KT, Qiu J, Su H-B, Watanabe T, Brunet Y (1995) Surface renewal analysis: a new
688 method to obtain scalar fluxes. *Agric For Meteorol* 74:119-137.

689 Raupach MR, Finnigan JJ, Brunet Y (1996) Coherent eddies and turbulence in vegetation
690 canopies: the mixing-layer analogy. *Boundary-Layer Meteorol* 78:351-382.

691 Renno NO, Abreu VJ, Koch J, Smith PH, Hartogensis OK, De Bruin HAR, Burose D, Delory
692 GT, Farrell WM, Watts CJ, Garatuza J, Parker M, Carswell A (2004) MATADOR

693 2002: A pilot experiment on convective plumes and dust devils. *J Geophys Res*
694 109:E07001.

695 Schols JJJ (1984) The detection and measurement of turbulent structures in the atmospheric
696 surface layer. *Boundary-Layer Meteorol* 29:39-58.

697 Schols JJJ, Jansen AE, Krom JG (1985) Characteristics of turbulent structures in the unstable
698 atmospheric surface layer. *Boundary-Layer Meteorol* 33:173-196.

699 Snyder RL, Spano D, Paw U KT (1996) Surface renewal analysis for sensible and latent heat
700 flux density. *Boundary-Layer Meteorol* 77:249-266.

701 Spano D, Snyder RL, Duce P, Paw U KT (1997) Surface renewal analysis for sensible heat
702 flux density using structure functions. *Agric For Meteorol* 86:259-271.

703 Spano D, Snyder RL, Duce P, and Paw U KT (2000) Estimating sensible and latent heat flux
704 densities from grapevine canopies using surface renewal. *Agric For Meteorol*
705 104:171-183.

706 Sparrow EM, Husar RB, Goldstein RJ (1970) Observations and other characteristics of
707 thermals. *J Fluid Mech* 41:793-800.

708 Tiselj I, Bergant R, Makov B, Bajsić I, Hestroni G (2001) DNS of turbulent heat transfer in
709 channel flow with heat conduction in the solid wall. *J Heat Transfer* 123:849-857.

710 Townsend AA (1959) Temperature fluctuation over a heated horizontal surface. *Fluid Mech*
711 5:209-241.

712 Vogt R (2008) Visualisation of turbulent exchange using a thermal camera. Paper no. 8B.1.
713 18th Symposium on Boundary Layer and Turbulence, Stockholm, Sweden.

714 Wilczak JM, Businger JA (1983) Thermally indirect motions in the convective atmospheric
715 boundary layer. *J Atmos Sci* 40:343-358.

716 Wilczak JM, Tillman JE (1980) The three-dimensional structure of convection in the
717 atmospheric surface layer. *J Atmos Sci* 37:2424-2443.

718 Wilczak JM, Oncley SP, Stage SA (2001) Sonic anemometer tilt correction algorithms.
719 *Boundary-Layer Meteorol* 99:127-150.

720 Wyngaard JC, Cote OR, Izumi Y (1971) Local free convection, similarity and the budgets of
721 shear stress and heat flux. J Atmos Sci 28:1171-1182.